Study of Snow Dynamics at Subgrid Scale in Semiarid Environments Combining Terrestrial Photography and Data Assimilation Techniques

RAFAEL PIMENTEL AND JAVIER HERRERO

Fluvial Dynamics and Hydrology Research Group, Andalusian Institute for Earth System Research, University of Granada, Granada, Spain

YIJIAN ZENG AND ZHONGBO SU

Faculty of Geo-Information Science and Earth Observation, University of Twente, Enschede, Netherlands

MARÍA J. POLO

Fluvial Dynamics and Hydrology Research Group, Andalusian Institute for Earth System Research, University of Córdoba, Córdoba, Spain

(Manuscript received 14 March 2014, in final form 15 October 2014)

ABSTRACT

Snow cover simulation is a complex task in mountain regions because of its highly irregular distribution. GIS-based calculations of snowmelt–accumulation models must deal with nonnegligible scale effects below cell size, which may result in unsatisfactory predictions depending on the study scale. Terrestrial photography, whose scales can be adapted to the study problem, is a cost-effective technique, capable of reproducing snow dynamics at subgrid scale. A series of high-frequency images were combined with a mass and energy model to reproduce snow evolution at cell scale (30 m × 30 m) by means of the assimilation of the snow cover fraction observation dataset obtained from terrestrial photography in the Sierra Nevada, southern Spain. The ensemble transform Kalman filter technique is employed. The results show the convenience of adopting a selective depletion curve parameterization depending on the succession of accumulation–melting cycles in the snow season in these highly variable environments. A reduction in the error for snow depth to 50% (from 463.87 to 261.21 mm and from 238.22 to 128.50 mm) is achieved if the appropriate curve is selected.

1. Introduction

Snow plays an important role in the hydrologic regime of mountainous catchments. In Mediterranean regions, significant variability in both meteorological variables and topographic features can be found (Diodato and Bellocchi 2007). This adds complexity to the task of monitoring and modeling the evolution of snow distribution, which determines the infiltration–runoff regime and the availability of water during the dry season.

Initially, a first approach to studying snowpack evolution is made by using simple empirical relationships between the snowmelt flux and selected meteorological variables (Kustas et al. 1994). However, in these areas, the marked annual, seasonal, and even weekly variability of temperature, wind, and rainfall make this a difficult approach to apply in practice, and energy and mass balance equations are usually needed to capture these highly variable conditions (Anderson 1976). Many physically based point models for the mass and energy balance in the snowpack have been developed over the last few decades (e.g., Jordan 1991; Marks and Dozier 1992; Tarboton and Luce 1996). However, the particular features of snow dynamics in Mediterranean regions (Sade et al. 2014; Schulz and de Jong 2004) make it difficult for their application in some areas. For example, some models focus on the vertical gradients in the snow column

Corresponding author address: Rafael Pimentel, Fluvial Dynamics and Hydrology Research Group, Andalusian Institute for Earth System Research, University of Granada, Edificio CEAMA, Av. del Mediterráneo s/n, 18006 Granada Spain.
E-mail: rpimentel@ugr.es

DOI: 10.1175/JHM-D-14-0046.1

and require complex information as input or calibration data (e.g., Jordan 1991), whereas in Mediterranean regions, depths higher than 1 m may be seldom found in many sites. Other detailed approaches (e.g., Marks and Dozier 1992) capable of reproducing highly variable conditions require the availability of densely monitored areas to be calibrated, which is not frequent in mountainous areas, especially at high altitudes. On the other hand, models with a smaller number of state variables (e.g., Tarboton and Luce 1996) are very efficient to simulate runoff from snow areas with less demand of data sources, but they may not adequately reproduce the snow evolution under patchy conditions or during short and intense melting periods because of a fixed time step in the calculation. Herrero et al. (2009) developed a point energy balance snowmelt–accumulation model at a Mediterranean site following the formulation proposed by Tarboton and Luce (1996), which adopts a variable time step during the calculation procedure to better represent the variability of the different snow cycles within the season in these regions. The model also considers the important loss of water resources from snow evaporation under such conditions (Schulz and de Jong 2004; Sade et al. 2014), which accounted for as much as 42% of the total snowfall in extreme years, and the significance of the longwave radiation flux emitted from the snowpack in the energy balance. In addition, the use of a specific parameterization of this term in this area improved the model performance (Herrero and Polo 2012) and highlighted the differences in the driving processes for snow dynamics between Mediterranean and higher-latitude regions.

These models can be applied over whole areas, taking into account the significant issues of scale that arise when applying point models throughout a distributed area. The most common problems include 1) the selection of an optimal gridcell size according to the physics of the studied processes and 2) the question of how to represent the subgrid variability, also taking into account the snow dynamics. Following Blöschl (1999), who affirms that an optimal cell size may not exist, the model element scale may in practice be dictated by practical considerations such as data availability to calibration and validation stages and the required resolution of the predictions. For the second question, a simple parameterization by means of depletion curves (DCs), which extends the point mass and energy balance calculation by using a relationship between one selected snow state variable and the snow cover fraction (SCF) over a fixed area (Luce et al. 1999), can be applied. The availability of distributed snow measurements limits the application of both solutions, with different needs for the associated spatial resolution.

Remote sensing is the best and sometimes only available distributed data source for medium- to large-scale studies. Different time and spatial scales of data can be found between satellites, with a decreasing spatial resolution for a given location as frequency increases, that is, NOAA daily images with 1 km × 1 km cell size, MODIS daily images with 500 m × 500 m cell size, or Landsat 16-day images with 30 m × 30 m cell size. These satellite sources are widely used for examining the evolution of snow cover extent on a medium to large scale (Painter et al. 2009; Herrero et al. 2011; Wang et al. 2014; Malik et al. 2014). In semiarid environments, the extremely variable conditions favor the particular distributed patterns of the snow, which usually appear as medium- to small-sized patches. Thus, spatial resolution constitutes a limiting factor, and Landsat has been the data source most recommended for studying snow evolution over these areas (Marks and Winstral 2001; Pimentel et al. 2012), sometimes being combined with MODIS data to fill in the time lapse at a daily scale. Nevertheless, Landsat spatial resolution is not always capable of capturing the variability of snow distribution during spring or the short melting cycles in dry years, in which small snow patches may persist during many weeks in early summer (Rosenthal and Dozier 1996; Pimentel et al. 2012; Sade et al. 2014).

Moreover, the selection of the most representative DCs to expand the physical snow models' calculations over grid cells in distributed studies depends on the local conditions, including topography, vegetation, and the dominant regimes of the weather variables; that is, it requires the availability of SCF local measurements. Terrestrial photography (TP) is a cost-effective technique, capable of reproducing snow dynamics at the cell scale when combined with the physical model approach and point measurements of other variables, such as snow depth. Different examples of parameterization of DCs have been proposed in the literature (Ferguson 1984; Buttle and Mc Donnell 1987; Luce and Tarboton 2004), and local SCF data from TP provide a basis for the adoption of a given curve or local parameterizations. Additionally, to a high and easily flexible spatial resolution, TP frequency can be fixed at subdaily scales and even change within the monitoring period to be adapted to the process significant scales without effort.

Nevertheless, the final simulation of the spatial evolution of the snowpack may not result in a satisfactory performance because of the high degree of heterogeneity of the snow and the usual lack of extended in situ time series of snow depth/cover to generate specific local DCs, and the need for not only simulating snow cover but also snow depth values. The complementary use of assimilation techniques can reduce uncertainty in the model forecast, considering that field data for additional snow variables are available. There are many examples of snow simulation using different assimilation techniques,

from simple methods such as direct insertion (DI; Liston et al. 1999; Malik et al. 2012) to more complex methods such as those derived from applications of Kalman filter (Kalman 1960). In this group, a wide range of methodologies are found: the original Kalman filter, mainly used as linear forecast model; the ensemble Kalman filter (EnKF; Evensen 1994), which constitutes a stochastic formulation of the original filter and simplifies the problem of the nonlinearity of the process; or the ensemble square root filter (ESRF; Pham 2001; Tippett et al. 2003; Ott et al. 2004), which does not perturb the observation and improves the computational time.

This work presents the potential of TP for capturing snow dynamics at the subgrid scale as an intermediate step between point and distributed snow modeling, when combined with physical modeling and point measurements. For this purpose, three different DC parameterizations proposed by Luce and Tarboton (2004) were tested at a mountainous site in southern Spain by means of the assimilation of SCF values obtained from TP into a physical snow model previously validated at the study site (Herrero et al. 2009). The ensemble transform Kalman filter (ETKF) technique, belonging to the ESRF group, has been used in this study. A cell size of 30 m × 30 m was selected in order to use the results in a further validation of the distributed model in the region through Landsat data.

The article is organized as follows. Section 2 describes the characteristics of the study site and the available data; section 3 introduces the different steps in the calculation structure (snowmelt–accumulation model, DC, TP analysis, and ETKF technique); sections 4 and 5 present the results and discussion, and, finally, the conclusions are drawn in section 6.

2. Study site and available data

This study has been carried out in the Sierra Nevada, southern Spain. This linear mountain range, with altitudes ranging from 1500 to 3500 m, runs parallel to the Mediterranean coast at a distance of 60 km. It is characterized by high altitudinal gradients and a modification of the mountain climate influenced by the surrounding Mediterranean conditions. It is usually covered with snow, at altitudes of over 2000 m, during winter and spring, and although the snowmelt season extends from April to June, the typically mild Mediterranean winters produce several accumulation–melting cycles before the final spring melting. Annual precipitation fluctuates widely and can range from 400 to 1500 mm, with a high spatial variability throughout the area due to topographic effects. The average temperature ranges from −5° to 5°C during the snow season, although minimum values of −20°C can be found at certain times in winter.

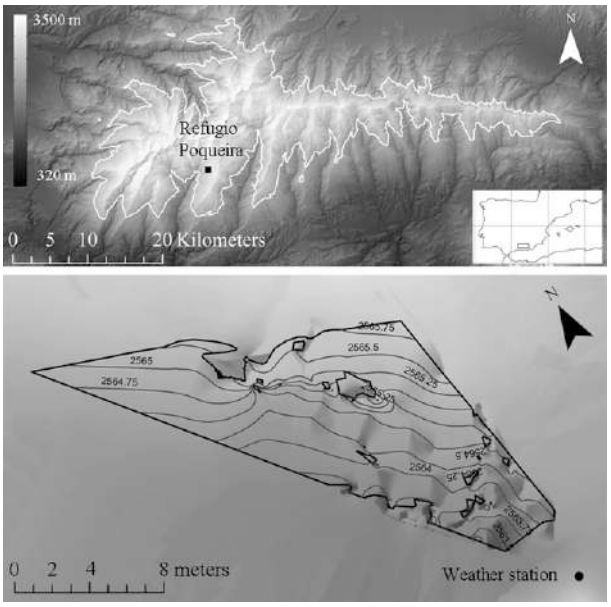

FIG. 1. (top) Location of the study site in the Sierra Nevada, southern Spain, and (bottom) DEM of the control area close to the Refugio Poqueira weather station. The black dot indicates the location of the weather station and the black solid line indicates the area covered by the images obtained from TP.

A control area of about 900 m^2 was selected near the monitoring weather station used in this study, Refugio Poqueira (Fig. 1), at 2500 m MSL. This area is composed of fragmented phyllites and schists, and a characteristic vegetation canopy, consisting of *Genista versicolor* and *Festuca clementei*, two compact and densely branched low shrubs that grow closely together, forming extremely compact, low, continuous cover, which acts as an insulator between the soil and the snowpack and is the main vegetation cover from 2000 to 2900 m over this area (Anderson et al. 2011).

a. Weather data

The automated weather station located at Refugio Poqueira (Fig. 1) consists of a rain gauge with Alter shields to facilitate snow collection, a pyranometer, a pyrgeometer, a temperature and humidity probe, a wind monitor, and a manometer. The 5-min datasets have been consistently recorded since 2004 up to the present; some statistical descriptors of the weather data at this site are included in Table 1. Table 2 shows the model and main characteristics of the instrumental components of the Refugio Poqueira station.

b. Terrestrial photography

Since the summer of 2009, an automatic CC640 Campbell Scientific camera has provided five images per day, every 2 h between 0800 and 1600 LT, of the control

TABLE 1. Statistics descriptors of selected meteorological variables at the Refugio Poqueira weather station during the study period (2009–11).

Variable	Unit	Mean	Max	Min
Annual precipitation	mm yr^{-1}	750	1250	467
Snowfall annual fraction (of annual precipitation)	%	60	70	40
Instant temp	°C	6.4	24.6	−14.4
Instant winter temp	°C	1.3	8.5	−14.4
Solar radiation	J m^{-2} day^{-1}	19.8×10^6	35.8×10^6	0.5×10^6
Wind speed	m s^{-1}	3.82	13.24	0.11

area, with a resolution of 640 × 504 pixels and a focal length of 85 mm. This camera is able to capture both the fast snow melting cycles and the spatial heterogeneity exhibited by the snow cover at the study site in relation to its microtopography. Additionally, two snow measuring rods were installed in the photographed area at representative points where the snow is more persistent during most of the accumulation–melting cycles throughout the year. Thus, the TP images allow us to monitor a representative snowpack depth at the study site with high-frequency recording.

c. Digital elevation model

A 0.05 m × 0.05 m digital elevation model (DEM) of the control area was derived from the spatial interpolation of topographic survey data. The topographic survey was designed from a previous analysis of the TP, from which the most important elements of the microtopography that condition the snow distribution over the control area were selected.

3. Methods

Two consecutive hydrologic years, 2009–11, were simulated at the study site by using the snow point model by Herrero et al. (2009), with three different DCs. The model was used with its original calibration, obtained with data from 2004 to 2007. Two different performances of the model were tested. First, the three DCs were evaluated by comparing TP-observed values of SCF and snow depth with their simulated results, without any assimilation procedure (open-loop simulation). Second, the TP-SCF dataset (observation) was assimilated by means of ETKF for the same DC formulations, and the simulated snow depth values were validated against the TP–snow depth dataset. This section describes the different items in the calculation process: the snow model structure, the three selected DCs, how the snow variables were obtained, and the ETKF assimilation technique.

a. Snow modeling: Point model

The snowmelt–accumulation model for Mediterranean sites developed by Herrero et al. (2009) is a physical model based on a point mass and energy balance. The model assumes a horizontally uniform snow cover distributed in one vertical layer. This snow column per unit area defines a control volume, with the atmosphere and the ground as external boundaries; the lateral mass and energy fluxes between adjacent snow columns are null since the horizontal gradients are neglected when compared to the vertical ones. The balance equations can then be expressed according to

$$\frac{d(\mathrm{SWE})}{dt} = P - E + W - M \tag{1}$$

and

$$\frac{d(u\mathrm{SWE})}{dt} = \frac{dU}{dt} = K + L + H + G + P(u_P) - E(u_E) + W(u_W) - M(u_M), \tag{2}$$

TABLE 2. Specifications of the sensors at the Refugio Poqueira weather station.

Instrument	Range	Operating temp (°C)
Campbell Scientific CR10X datalogger		From −25 to 50
Geonor T-200B rain gauge	0–600 mm	From −25 to 70
Vaisala HMP45C (temp)	From −40° to 60°C	From −40 to 60
Vaisala HMP45C (humidity)	0.8%–100%	From −40 to 60
Kipp and Zonen SP-Lite pyranometer	0.4–1.1 μm	From −30 to 70
Druck RPT410F barometer	600–1100 hPa	From −40 to 60
Young 05103-45 wind monitor	0–60 m s^{-1}	From −50 to 50
Pyrgeometer	4.5–44 μm	From −40 to 80

where snow water equivalent (SWE) is the water mass in the snow column, u is the internal energy per unit of mass (U for total internal energy), and t represents the time. In the mass balance, P defines the precipitation rate, E is the flux of water mass exchange with the atmosphere (positive for evaporation from the snowpack and negative for condensation from the atmosphere), W represents flux of water mass transport due to wind, and M is the melting water flux. In addition, for the energy fluxes in Eq. (2), K is the net solar or shortwave radiation flux; L is the net thermal or longwave radiation flux; H is the flux of sensible heat exchange with the atmosphere; G is the flux of sensible heat exchange with the ground; and u_P, u_E, u_W, and u_M are the unitary energy values associated with each one of the mass fluxes involved in Eq. (1). The terms $W(u_W)$ and $M(u_M)$ are advective and $E(u_E)$ and H are diffusive transport, whose formulation requires some characterization of the turbulent atmospheric conditions (Anderson 1976; Jordan et al. 1999). SWE values are transformed into snow depth values by means of a local empirical relationship for the experimental measurements.

Some simplifying assumptions were proposed when applying Eqs. (1) and (2) at the study site. The wind transport term W was disregarded because of the quick snow metamorphosis, which compacts the snow and reduces its mobility. The variable G was also disregarded since, besides being considered a secondary term per se in the energy balance (Kuusisto 1986), its value is considerably reduced at this site by the insulating properties of the local vegetation canopy. The variable P is direct input from the dataset measured by the weather station. In addition, K, L, $E(u_E)$, and H can be explained as

$$K = K\downarrow + K\uparrow = K\downarrow(1-\alpha), \tag{3}$$

$$L = L\downarrow + L\uparrow = L\downarrow - \sigma_{SB}T_{sn}^4, \tag{4}$$

$$U_E = \left(\frac{K_{U_E}}{\phi_M\phi_V}v_a\right)(e_{sn} - e_a), \tag{5}$$

and

$$H = \left(\frac{K_H}{\phi_M\phi_H}v_a + K_{H_0}\right)(T_a - T_{sn}), \tag{6}$$

where $K\downarrow$ and $K\uparrow$ are downwelling and upwelling shortwave radiation fluxes, $K\downarrow$ is measured directly by the weather station; α is the snow albedo, which in this study is considered to be constant with a value of 0.8; $L\downarrow$ and $L\uparrow$ are downwelling and upwelling longwave radiation fluxes, where $L\downarrow$ is also measured directly by the weather station; σ_{SB} is the Stefan–Boltzmann constant; $U_E = E(u_E)$; K_{U_E} is the bulk latent heat transfer coefficient, which depends on average roughness of the snow z_0; K_H is the bulk sensible heat transfer coefficient with wind and K_{H_0} is the same without wind; v_a, e_a, and T_a are the wind speed, the air vapor pressure, and the air temperature at a reference altitude z_R (typically 2 m), respectively; e_{sn} is the saturation vapor pressure for the snow temperature T_{sn}; and ϕ_M, ϕ_V, and ϕ_H are the stability-correction factors for nonadiabatic temperature gradients for mass, wind, and sensible heat, respectively (Dingman 2002). In this work, the conclusions from Herrero et al. (2009) for snow dynamics at the study site were adopted, with values of 6 W m^{-2} K^{-1} for K_{H_0} and 2.5 mm for z_0, and the terms ϕ_M, ϕ_V, and ϕ_H were disregarded.

b. Depletion curve

DCs are used to expand the point snow calculations over the cell size area selected as a previous step in the distributed modeling of the snowpack, taking into account the spatial variability at the subgrid scale. These empirical functions relate the SCF (the fraction of cell area covered by the snow) to other snow variables. During an accumulation–melting cycle, the selected DC includes the decrease in snow cover within the cell area and therefore affects the quantification of energy fluxes in the energy balance. These fluxes are reduced proportionally to the fraction of the area covered by the snow. Thus, it is important to select a suitable DC when applying the model.

Different methodologies have been employed to define these curves. For example, Cline et al. (1998) used remote sensing data to generate DCs under the assumption that the SCF decrease over time was spatially coherent—in other words, the snow did not change its location. Luce and Tarboton (2004) employed a probability density function of SWE for the peak accumulation date over a basin, and Kolberg and Gottschalk (2006) applied a Bayesian approach to update these curves using remote sensing data. However, most of the DCs proposed relate SCF and SWE, with rare exceptions.

Following this, the DC shapes proposed by Luce and Tarboton (2004) from different distribution functions were tested at the study site to select the formulation that most closely resembled most of the in-season melting cycles that characterize snow dynamics in Mediterranean climates. A lognormal distribution was finally chosen. Three parameterizations described by their coefficient of variation (CV) were adopted for a lognormal distribution between the dimensionless variables of snow water equivalent, SWE* (SWE* = SWE/SWE$_{max}$, where SWE$_{max}$ is the SWE maximum in each melt cycle), and SCF in the control area (Fig. 2).

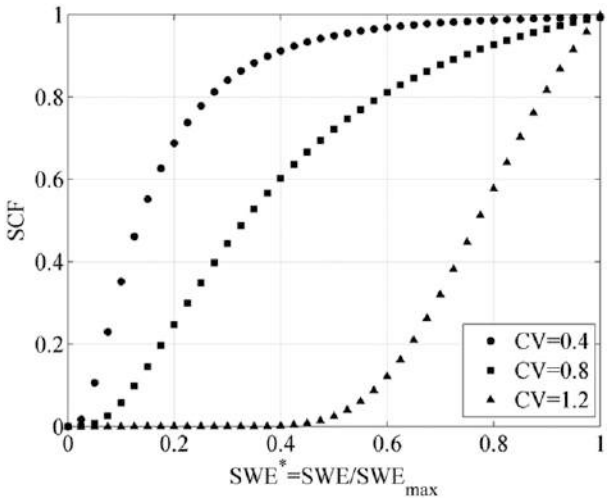

FIG. 2. Different dimensionless DCs parameterized as lognormal distribution for different CVs.

The CV represents the main trend in the evolution of areal accumulation–melting. Lower values were associated with a higher sensitivity of SCF to changes in SWE* in the first stage of the accumulation and in the last stage of melting processes, whereas high CV values correspond to low sensitivity of SCF during the initial stages of snow accumulation but with quick changes in SCF during the initial stages of melting. At the spatial scale of the present study (30 m × 30 m), the snow properties, together with the microtopography and ground vegetation at a given site, among others, are the underlying factors for a given DC shape representing local conditions.

c. *Terrestrial photography analysis*

To quantify the evolution of snow at the subgrid scale, TP observations were obtained at the study site during two consecutive hydrologic years (2009–11). Every TP image underwent a two-step analysis: georeferencing, to provide the image with spatial coordinates, followed by a snow detection process using a nonsupervised clustering algorithm, which provided both the SCF and snow depth for each image. Both steps are described below.

1) GEOREFERENCE

The georeference of each image was made on the basis of the local DEM, whose quality together with the image quality (level of distortion induced by the lens during the acquisition process) determined the final accuracy of the results.

First, the images were lined up to correct possible displacements during the acquisition process. Second, the corrected images were georeferenced to a DEM following standard procedures for viewing with computer graphics (Fiume 1989; Foley et al. 1990), which relate the two-dimensional pixels in the images to the three-dimensional points in the DEM. This mapping function translates the coordinate system of the DEM to the camera position and applies a transformation according to the focal length and view direction. The result is a virtual photograph of the DEM, that is, a representation of it as it would be seen from the point of view of the camera. The two-dimensional representation of the DEM is then scaled according to the resolution of the photograph (Corripio 2004; Rivera et al. 2008). In this way, the two representations can be superimposed, establishing the necessary correspondence between a pixel in the photograph and its projection coordinates in the DEM. The final result is a map in which all the pixels in the TP have been located over the terrain.

2) SNOW DETECTION

To distinguish the snow-covered and noncovered pixels in each image, a clustering algorithm was applied. These unsupervised methods are generally used to group together data according to some certain notion of similarity. In this case, all the white points in the scene are linked to the presence of snow, so that two clusters can be easily defined: snow-covered and noncovered pixels. A *K*-means clustering (MacQueen 1967) was selected; this algorithm classifies the data into a given number of clusters, selecting a random center within each cluster and minimizing the distance between the data and these centers. This algorithm proved to be efficient enough to differentiate these two kinds of pixels, since it was capable of detecting most of the snow area with no previous calibration or the use of fixed thresholds in the images, with a resulting low level of misclassifications, which were in turn related to the presence of strong shadows in the images (Pimentel et al. 2012). From this pixel classification, the SCF can be easily calculated.

This algorithm was also used to measure the snow depth from the rods installed in the control area. The rods were painted in a distinct color, red, which made them easy to differentiate from the remaining objects in the scene. From the clustered results, a linear equation was capable of estimating the depth of the snow from the identified pixels with rods.

d. *Ensemble transform Kalman filter*

As stated before, the data assimilation method employed in this work is the ETKF. This filter was introduced by Bishop et al. (2001) as a form of square root filter that allows a deterministic update of the ensemble anomalies (Tippett et al. 2003), and it is usually chosen for its natural characteristics and its computational efficiency (Sakov and Oke 2008). It is based on

the equations of the Kalman filter and the Monte Carlo perturbation of the EnKF.

The Kalman filter analysis equations represent the state variable update from the assimilation process, and they can be described as

$$\mathbf{x}^a = \mathbf{x}^f + \mathbf{K}(\mathbf{d} - \mathbf{H}\mathbf{x}^f), \tag{7}$$

where $\mathbf{x}^a$ is the analysis and $\mathbf{x}^f$ is the forecast; $\mathbf{d}$ is the vector observation; $\mathbf{H}$ is the operator mapping the state vector space to the observation space; and $\mathbf{K}$ is referred to as the Kalman gain, given by

$$\mathbf{K} = \mathbf{P}^f\mathbf{H}^{\mathrm{T}}(\mathbf{H}\mathbf{P}^f\mathbf{H}^{\mathrm{T}} + \mathbf{R})^{-1}, \tag{8}$$

with $\mathbf{P}^f$ and $\mathbf{R}$ being the forecast and observation error covariance matrices, respectively. The superscripts f and a denote forecast and analysis, respectively, and the superscript T denotes a matrix transpose.

These are the basic equations also used by EnKF, but this one employs a Monte Carlo approximation to solve the problem of the nonlinearity of the model used. The covariance matrix $\mathbf{P}$, in this case, is stored and manipulated implicitly via an ensemble variable $\mathbf{X}$ of the model states, $\mathbf{X} = [\mathbf{X}_1, \ldots, \mathbf{X}_m]$, with m being the ensemble size and with the square brackets indicating a range of values, by means of the relationship

$$\mathbf{P} = \frac{1}{m-1}\sum_{i=1}^{m}(\mathbf{X}_i - \mathbf{x})(\mathbf{X}_i - \mathbf{x})^{\mathrm{T}} = \frac{1}{m-1}\mathbf{A}\mathbf{A}^{\mathrm{T}}, \tag{9}$$

where $\mathbf{x}$ is the ensemble mean

$$\mathbf{x} = \frac{1}{m}\sum_{i=1}^{m}\mathbf{X}_i \tag{10}$$

and $\mathbf{A} = [\mathbf{A}_1, \ldots, \mathbf{A}_m]$ is the ensemble of the individual anomalies or perturbations,

$$\mathbf{A}_i = \mathbf{X}_i - \mathbf{x}. \tag{11}$$

Based on these equations, Sakov et al. (2010) defined the ETKF by rewriting the general analysis equation given by Eq. (6) in a generic form:

$$\mathbf{x}^a - \mathbf{x}^f = \mathbf{A}^f\mathbf{G}\mathbf{s}, \tag{12}$$

where $\mathbf{s}$ is the scaled innovation vector, defined as

$$\mathbf{s} = \mathbf{R}^{-1/2}(\mathbf{d} - \mathbf{H}\mathbf{x}^f)/\sqrt{m-1}, \tag{13}$$

and $\mathbf{G}$ stands for

$$\mathbf{G} = \mathbf{S}^{\mathrm{T}}(\mathbf{I} + \mathbf{S}\mathbf{S}^{\mathrm{T}})^{-1}, \tag{14}$$

with $\mathbf{S}$ being the term that represents the scaled ensemble observation anomalies:

$$\mathbf{S} = \mathbf{R}^{-1/2}\mathbf{H}\mathbf{A}^f/\sqrt{m-1}. \tag{15}$$

In this annotation, the anomalies of the ensemble update are calculated as

$$\mathbf{A}^a - \mathbf{A}^f = \mathbf{A}^f\mathbf{T}, \tag{16}$$

with $\mathbf{T}$ being the transform matrix for ETKF proposed by Bishop et al. (2001):

$$\mathbf{T} = (\mathbf{I} + \mathbf{S}^{\mathrm{T}}\mathbf{S})^{-1/2} - \mathbf{I}. \tag{17}$$

In this work, the platform EnKF-Matlab (version 0.28) developed by Sakov (http://enkf.nersc.no/Code/EnKF-Matlab/) was used to implement the aforementioned development of ETKF.

Two aspects must be taken into account to apply the ETKF: model error estimation and optimal ensemble size. In that case, because of the deterministic aspect of the filter, observation error estimation is not considered.

The determination of model errors remains a largely subjective issue, as it is very difficult to attribute the error to the physics of the model (Reichle 2008). One way to quantify this model error is by including the uncertainties in both the forcing of the data and the model formulation (Reichle 2008). In this study, a representative value of the variability was employed to perturb the forcing parameters. Considering that the time resolution of the meteorological data was 5 min and according to the time step of the modeling, 1 h, the standard deviation of the data was calculated every hour. The 90th percentile of the standard deviation sample obtained was selected as the representative value to perturb all the meteorological inputs, with the exception of precipitation. In this case, when the measured precipitation was zero, no perturbation was performed; the rest of the measured values were divided into three intervals, whose limits depended on the amount of precipitation, and a standard deviation was calculated for each one. Table 3 shows the different representative values employed for perturbing each weather variable.

To select the optimal ensemble size, different simulations with ensembles of 10, 20, 50, 100, and 200 members were performed. The ensemble size that minimized the root-mean-square error (RMSE) between observation and simulation was finally adopted as the optimal one. The RMSE for a given ensemble size was calculated as the mean of the RMSE of the simulation of three different DCs performed.

TABLE 3. Representative values used to perturb the different meteorological variables used in the modeling.

Meteorological input	Unit	Representative value
Temp	°C	0.663
Emissivity	%	10.00
Wind speed	$m\,s^{-1}$	1.363
Air pressure	kPa	0.049
Air relative humidity	%	6.65
Radiation	$J\,m^{-2}\,s^{-1}$	110.5
Precipitation		
$P = 0$	mm	No perturbation
$0 < P < 2$	mm	0.496
$2 \leq P < 5$	mm	0.810
$P \geq 5$	mm	2.568

4. Results

a. Snow variables measured

About 2000 images from the study period, the two hydrologic years 2009/10 and 2010/11, were georeferenced using the DEM obtained in the control area. The results of this process were snow cover maps in the photographed areas, with the same spatial resolution of the DEM (0.05 m × 0.05 m) and with the same temporal resolution of the image acquisition process (five images per day). Figure 3 shows different examples of this georeference process.

As can be observed, the snow was correctly detected at different times of the year under different weather conditions: on clear days at the beginning of the snowy season (9 December 2010); on days with a total snow cover and the appearance of shadows (6 February 2011); or on days with a morning mist at the end of the fusion periods (2 May 2011), which confirmed the usefulness of TP at the scale of the work analyzed. Table 4 shows some statistics of the snow state variables measured using these images.

Moreover, the high temporal resolution of TP allowed the monitoring of some characteristic fast evolution that usually takes place in this area, mainly during the melting season. Figure 4a shows the average hourly rate of change in SCF, with the highest rate from autumn initial snow and spring melting of the second year, a maximum value of $0.065\,m^2\,m^{-2}\,h^{-1}$ (26 November 2010); the medium range was from some winter period and spring melting of the first year, with a maximum rate of $0.025\,m^2\,m^{-2}\,h^{-1}$ (24 April 2010). Both greatly contrast with periods with negligible values during some winter periods. Figure 4b includes a comparison between TP-SCF values (small black

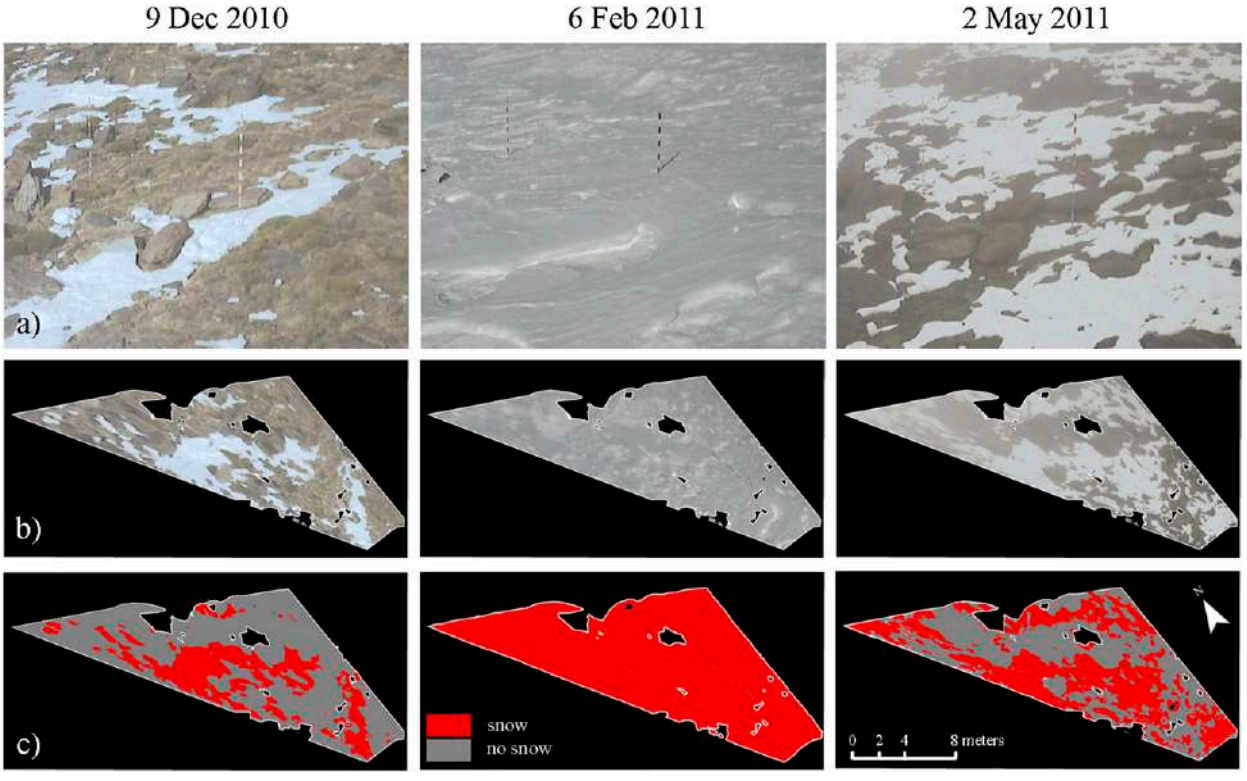

FIG. 3. Example of the TP georeference process on the study site for selected days during the snow season: (a) original image, (b) georeferenced image, and (c) snow mask obtained from the georeferenced image by using the simple *K*-means algorithm described in section 3b(2).

TABLE 4. Statistics descriptors of the snow state variables measured using TP.

Snow depth (mm)		SCF	
Min	0	Days completely covered by snow	162
Max	1400	Days completely free of snow	73
Mean in days with snow	612.9	Days partially covered by snow	401
Std dev in days with snow	125.2	Days without information	94

dots) and SCF values obtained from different remote sensing sources in the study area at the adequate scale and given dates: 1) Landsat, providing covered and noncovered pixel classification from normalized difference snow index (NDSI) values (gray dots), and 2) MODIS, providing SCF from the MOD10A1 product (black crosses). In general, none of them is able to reproduce the global variability exhibited by snow during given periods, which can be observed from TP. MODIS-SCF values, which covered a greater extension than the cell size, match TP observations during covered periods but not during the melting season (e.g., spring melting cycle of 2010, which is prolonged by MODIS for approximately 1 month); on the contrary, Landsat classification reproduced this period best, but its temporal resolution clearly limited the monitoring of quick changes (e.g., the absence of data during the spring melting of the second year). The potential of TP observations as a complementary data source to these remote sensing sources can be clearly observed.

b. *Open-loop simulation*

Figures 5 and 6 show the evolution of SCF and snow depth, respectively, simulated by the snow model for the three DCs used and their comparison with the TP measurements; dispersion graphs are also included in the figures.

The SCF open-loop simulation (Fig. 5) produced similar trends for every DC. As a general trend, the DCs with CV = 0.4 and 0.8 reproduced, with a high approximation, the behavior of the snow during the whole period with RMSE = 0.151 and 0.145 $m^2 m^{-2}$, respectively. They were even capable of capturing small fusion–accumulation cycles at the beginning and end of the season. The DC with CV = 1.2 also reproduced long periods with persistent snow adequately, however, could not approximate those short, intense cycles at the beginning and end of the annual snow period. A larger error (RMSE = 0.190 $m^2 m^{-2}$) than previous DCs for the study period was found.

A similar behavior can be observed for the simulated snow depth evolution (Fig. 6). As a general trend, the DCs with CV = 0.4 and 0.8 underestimate the depth of the snow. During the two years selected, both reproduce with a reasonable approximation the snow depth during the snow season up to the beginning of the spring accumulation period. From then on, both curves give rise to greater fusion fluxes than those observed, mismatching the measured and simulated snow depth results. Conversely, the curve with CV = 1.2 overestimates the depth in a generalized manner during the study period, and even generates the presence of snow during the summer season, when no snow is observed.

c. *TP-SCF assimilation simulation*

TP-SCF values were used as the observation dataset in the assimilation process. First, the ETKF was calibrated

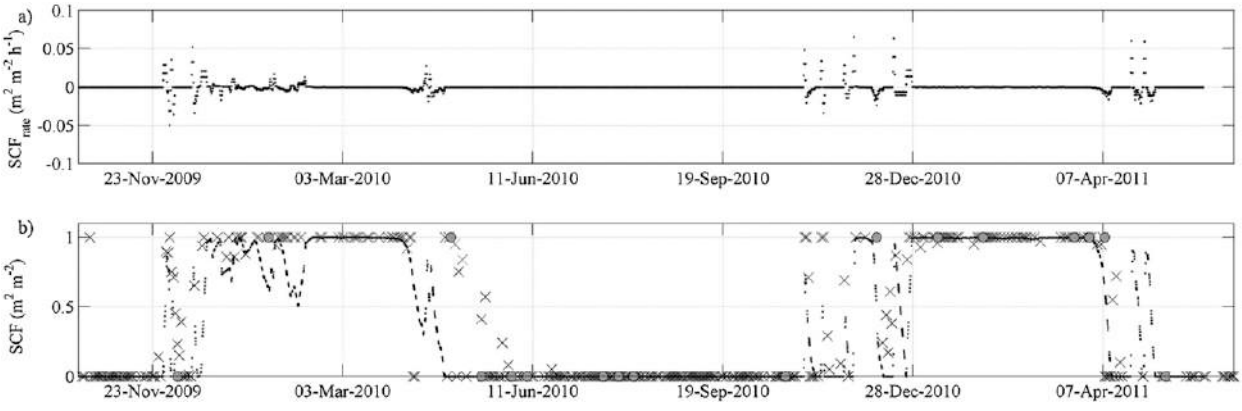

FIG. 4. (a) Average hourly rate of change in SCF throughout the study period. (b) Comparison between SCF obtained from TP (black dots) and SCF obtained from Landsat (gray dots) and MODIS (black crosses).

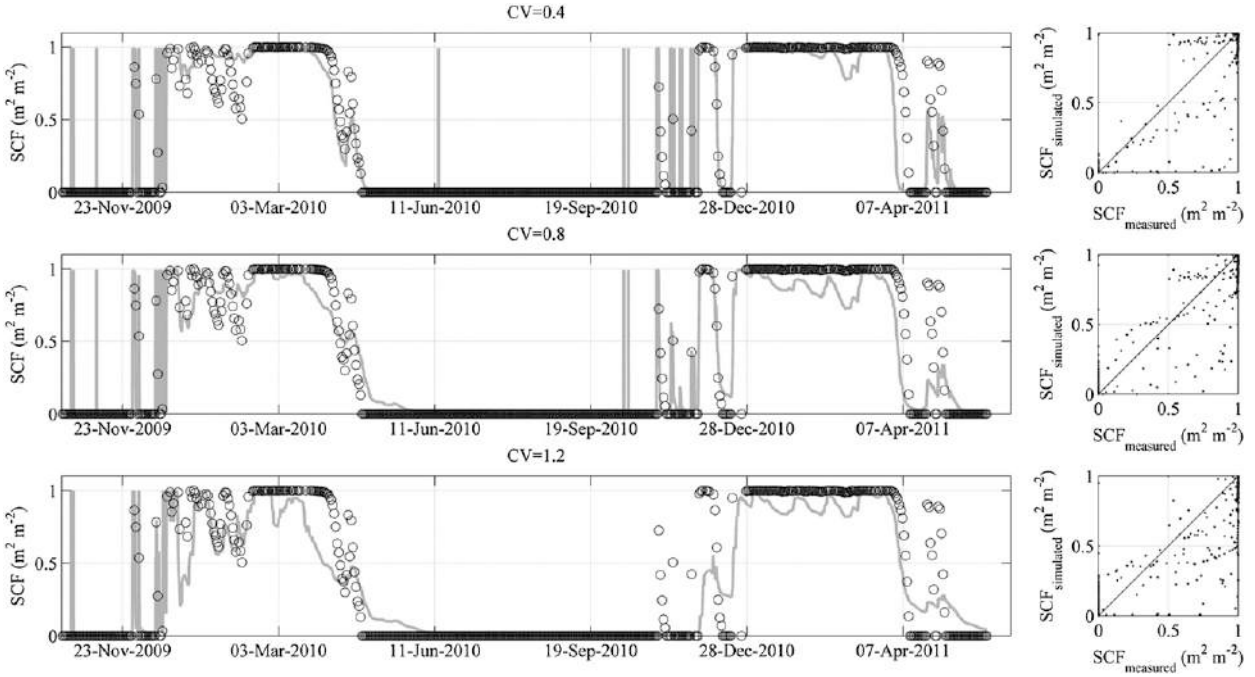

FIG. 5. (left) Measured (black dots) and simulated open-loop (gray line) SCF evolution for each DC used by the snow model without assimilation. (right) Dispersion graphs between measured and simulated SCF.

by minimizing the mean RMSE values associated with each DC for a different number of ensemble members (Table 5). It can be seen how the greater the size, the smaller the error, with very significant improvements in the simulation at the beginning of the interval of sizes evaluated (e.g., the error produced was reduced to almost one-third depending on whether a filter of 10 or 20 members was selected), and a certain stabilization of its

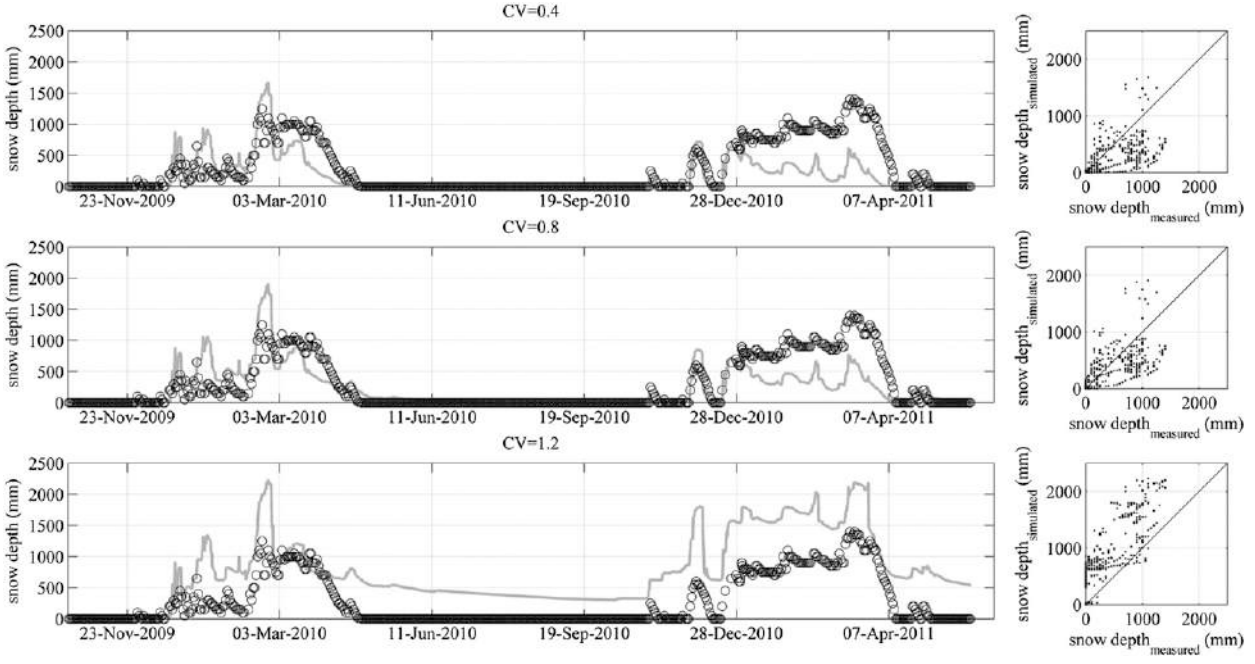

FIG. 6. (left) Measured (black dots) and simulated open-loop (gray line) snow depth evolution for each DC used by the snow model without assimilation. (right) Dispersion graphs between measured and simulated snow depth.

TABLE 5. RMSE values for SCF estimations with different ensemble sizes. For a given size, the RMSE is calculated as the averaged RMSE values associated with each DC.

Ensemble size	$RMSE_{SCF}$ ($m^2\,m^{-2}$)
10	0.351
20	0.257
50	0.248
100	0.251
200	0.253

value as from a certain size threshold was noted. In view of these results, a size of 20 members was chosen as being optimal for the goodness of the simulation and the associated computational cost, since, starting from this value, the diminution of the associated error was hardly noticeable [$O(\sim 0.01)\ m^2\,m^{-2}$ for the SCF].

The simulated snow depth values were tested against the independent snow depth observations (Fig. 7), with a decrease in the RMSE values in all the cases when compared to the open-loop simulations (Table 6 and Figs. 6, 7), especially for CV = 0.4 and 0.8 curves. However, it should be pointed out that, in spite of this global improvement, the assimilation was not able to reproduce the snow depth (Fig. 7) with the same degree of approximation for all the accumulation–melting cycles during the study period. This is clear in the case of the DC with CV = 1.2, in which snow presence during the summer season continues to be simulated without actually being observed, resulting in high global RMSE values. Also, CV = 0.4 and 0.8 curves reproduced the initial and final stages of every annual snow season better, but failed to simulate some intermediate periods, with significant differences between both curves depending on the season and cycles being analyzed. On the whole, despite the major improvement experienced in the three DCs analyzed, the DC with intermediate CV (CV = 0.8) was the one that best represented the observations, with an RMSE value of 191.18 mm over the whole study period (equivalent to 30% of the mean snow depth), against the 279.23 and 523.14 mm values obtained for CV = 0.4 and 1.2, respectively (equivalent to 45% and 85% of the mean snow depth, respectively).

TP-SCF assimilation has allowed both the analysis of the DC that best reproduced the snow dynamics at the subgrid scale and the improvement in the physical model performance. The incorporation of these observations in the modeling by ETKF led, in all cases, to a reduced error in the modeling, situating it within acceptable ranges. To evaluate the degree of improvement of the assimilation in the modeling, a dimensionless performance index, IND_{Perf}, was defined as

$$IND_{perf} = \frac{RMSE_{without\ assimilation} - RMSE_{with\ assimilation}}{RMSE_{without\ assimilation}}, \quad (18)$$

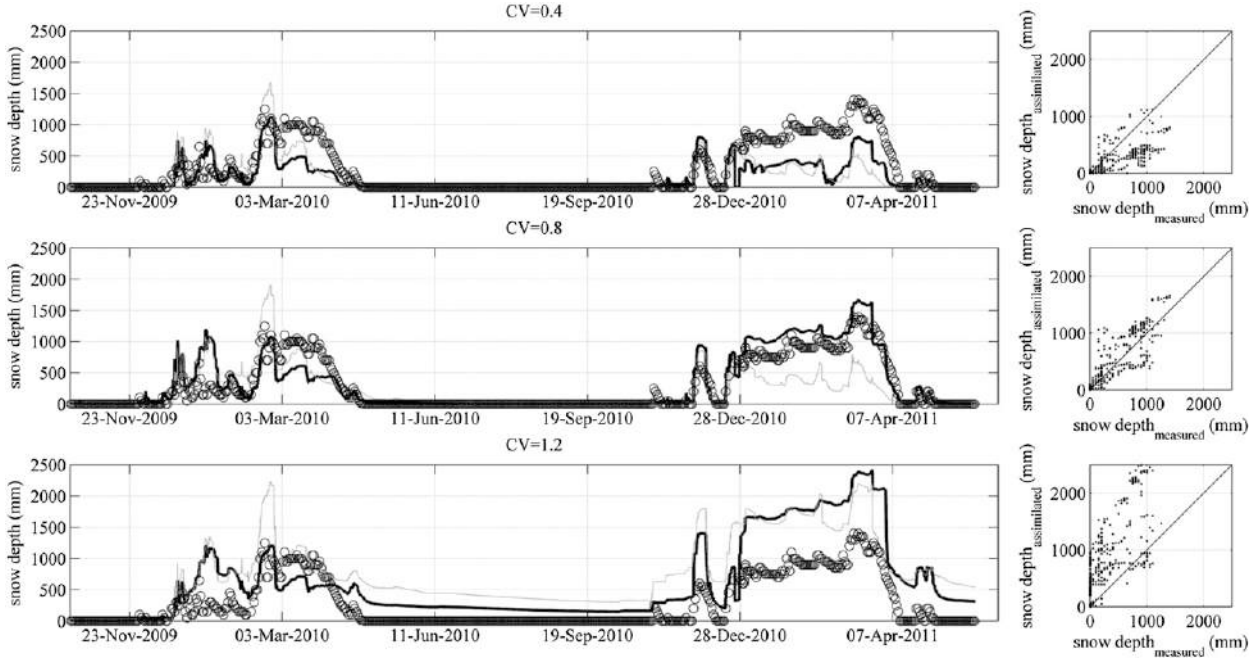

FIG. 7. (left) Measured (black dots), simulated (gray line), and ETKF-assimilated (black line) snow depth evolution for each DC used by the snow model. (right) Dispersion graphs between measured and assimilated snow depth.

TABLE 6. RMSE associated with the comparison between model-assimilated and TP-measured values of snow depth for each DC in the open-loop and TP-SCF assimilation simulations.

	CV = 0.4	CV = 0.8	CV = 1.2
$RMSE_{\text{snow depth, open-loop simulation}}$ (mm)	321.26	285.37	555.96
$RMSE_{\text{snow depth TP-SCF assimilation simulation}}$ (mm)	279.23	191.18	523.14

where $RMSE_{\text{without assimilation}}$ and $RMSE_{\text{with assimilation}}$ are the errors between observed and simulated values of snow depth with and without assimilation, respectively; this index typically ranges between 0 and 1, with increasing values for the higher degrees of improvement. For the three DCs studied, the assimilation improved the simulated values of the snow depth over 25%, with IND_{Perf} values of 0.13, 0.39, and 0.05 for the curves with CV = 0.4, 0.8, and 1.2, respectively. Obviously, a greater improvement was observed for the simulated SCF values, since this variable was directly assimilated, with IND_{Perf} values of 0.60, 0.66, and 0.50, respectively, for each curve, these results being an indirect indicator of the correct implementation of the methodology.

5. Discussion

The results shown in the previous section demonstrate the importance of selecting one of the DCs in order to model the snow state variables correctly. The shape of these curves is closely related to the physics of the process. Hence, the curve of the highest CV (CV = 1.2) represents a very fast initial melting process, which slows down in its final stage, leaving important amounts of snow concentrated in small areas of land. This could explain the overestimation of the depth produced during the summer season, which, in turn, conditions the results of the second year, so that the use of this DC to parameterize subgrid variability was disregarded. In contrast, the other curves with lower CV values (CV = 0.4 and 0.8) enable the snow to stay longer, cover a larger area, and produce fast melting after crossing a certain threshold, which seems to be more adequate for the conditions at the study site. According to the RMSE values shown in Table 6, the DC with CV = 0.8 represents the best global performance of the snow model. Nevertheless, in Fig. 7, different trends can be observed between both simulations depending on the type of accumulation–melting cycle throughout the year. To address this, two different situations were identified during the study period, and the RMSE values associated with each of them were calculated: 1) short accumulation–melting cycles that are associated with sporadic snowfall occurrence at the beginning and end of the hydrologic year, usually over nonhighly covered conditions, and 2) large accumulation–melting cycles during the central part of the snow season. Table 7 shows the RMSE values calculated for both DCs during each cycle period. Hence, in spite of the similarity between both DCs, small aspects can be differentiated. The DC with CV = 0.4 produces faster decreasing rates than the DC with CV = 0.8 and is capable of reproducing short accumulation–melting cycles, but it cannot maintain the snow presence until the end of the melting period. The RMSE for snow depth is reduced by up to approximately 50% for both types of conditions when the appropriate curve is selected (Table 7). Moreover, these trends are closely related to the conditions of the state of the snow that can be found during each kind of cycle. The snow is usually slightly compacted during short cycles and much more metamorphosed and compacted during longer cycles, especially at the end stages. These results point to the convenience of adopting a selective DC parameterization depending on the succession of accumulation–melting cycles in the snow season in these highly variable environments.

Following this, an optimal performance of the assimilation modeling process could be obtained by selecting the CV = 0.4 curve from November 2009 to early March 2010, and shifting to the CV = 0.8 until the end of this hydrologic year, to recover the CV = 0.4 curve for the initial sporadic snowfall events and then the CV = 0.8 curve from the end of December 2010 onward. The assimilation process made it possible to overpass the initial overestimation of the simulated snow depth values during the short cycles in 2009 and the initial stage of the long cycle in the winter of 2010 (Fig. 5), with any DC, resulting in a really high approximation when the CV = 0.4 curve was adopted and TP-SCF values were assimilated (Fig. 7). Similarly, the initial underestimation of the simulated snow depth values during the long, persistent cycle in winter and spring of 2011 (Fig. 6) was

TABLE 7. RMSE associated with the comparison between model-assimilated and TP-measured values of snow depth and SCF for each DC and for different snowmelt–accumulation periods.

	CV = 0.4	CV = 0.8
$RMSE_{\text{snow depth large periods}}$ (mm)	463.87	261.21
$RMSE_{\text{snow depth short periods}}$ (mm)	128.50	234.22

greatly improved by the CV = 0.8 curve and the assimilated TP-SCF values. Analyzing the terrestrial images and the weather data during both periods (Fig. 8), it can be observed that for the first periods (an example is shown in Fig. 8a) the wind recorded during the night of 19 February and the morning of 20 February 2010 (mean velocity of 15 m s^{-1}) redistributes the snow in the area, with a decrease of 500 mm. For the second period selected (Fig. 8b), the precipitation in the form of snow taking place (35 mm) is not sufficient to justify the increase in depth observed in the measurements on 31 December 2010 (300 mm), nor is the temperature high enough to cause the subsequent decrease observed on 1 January 2011 (100 mm). However, the intensity of the wind recorded on those days (8 m s^{-1}) reached fresh and not yet consolidated snow, causing its important redistribution. The snow model used does not incorporate the redistribution action caused by the wind (see section 3a) and therefore does not reproduce those variations in snow depth that are fundamentally due to this agent. The assimilation of TP-SCF data is able to partially correct this absence of wind transport in the physical model, as shown by the ETKF-simulated snow depth values for those conditions (Fig. 7).

However, despite these considerations, some significant mismatches in the simulation of snow depth still persisted during the spring of 2010 and, to a lesser extent, in the winter of the 2010/11 hydrologic year in the ETKF simulations (Fig. 7). An additional explanation for this could lie in the performance of the snowfall occurrence simulation made by the model, as the detailed joint analysis of the weather dataset and the TP observations seem to indicate, but no further conclusions can be derived from the present results. All in all, the usefulness of TP data for analyzing the variability of snow at the subgrid scale and improving the physical model performance has been highlighted, in terms not only of SCF assimilation values and DC selection, but also of gaining insight into the significant processes at high-resolution time scales in these variable semiarid environments.

6. Conclusions

The use of TP to study the evolution of snow cover has permitted the continuous monitoring of that layer, adapted to the spatial and temporal scale of the physical processes, and has proved to be a simple and economical way to obtain detailed measurements both of SCF and of snow depth. This study shows that disposing of this type of information is especially relevant in highly variable environments like the Mediterranean, in which the great heterogeneity presented by the snow layer requires detailed analysis at a local scale, during given periods whose conditions cannot be captured by conventional remote sensors alone. Specifically, the TP observations allowed the assessment of DC parameterizations over the study site.

The incorporation of this detailed information into the snow modeling process by means of the data assimilation technique selected, ETKF, significantly improved the simulations of snow dynamics at the subgrid scale made with the physical accumulation–melting snow model previously calibrated at the study site. This prevented some of the mismatches that occur at certain moments during the snow season under either highly variable conditions or processes not explicitly included in the physical modeling, which are then extended over the rest of the season, thus affecting the overall goodness of the simulation. The TP-SCF assimilation has permitted us to choose the DC that best reproduces the fusion processes taking place in this type of environment from those proposed in the literature. In this pilot area selected in the Sierra Nevada (Spain) in particular, two optimal curves have been identified to better reproduce the change rate of snow variables depending on the kind of cycle taking place and the presumably associated characteristics of the snow, consolidated or not-so-consolidated, with the CV = 0.8 and 0.4 DCs proposed by Luce and Tarboton (2004) associated with each snow state, respectively. Both curves allowed the total cover of the area to be maintained during the first melting process stages, increasing the speed of the melting process in its intermediate stage, and keeping a small fraction covered in its final stage. Nevertheless, over the whole study period, the CV = 0.8 curve performed better in the simulations both with and without TP-SCF values assimilation. However, the results point to the adoption of a selective curve procedure depending on the occurring snow cycle as the optimal simulation process.

This type of dynamics is associated, on the one hand, with the type of local microrelief, and, on the other, with the order of magnitude of the maximum depth of snow accumulated during the annual period. Despite the improvement produced when significant snow transport events occur because of the action of the wind, the TP-SCF values assimilation is not always capable of sufficiently mitigating the mismatch of the modeling for given periods. Further analyses should be made to identify the reasons behind this fact. This demonstrates the importance of this atmospheric conditioning for modeling the snow layer in these highly variable situations. It also indicates the usefulness of having DCs derived directly from local observations under these conditions available, as well as of implementing

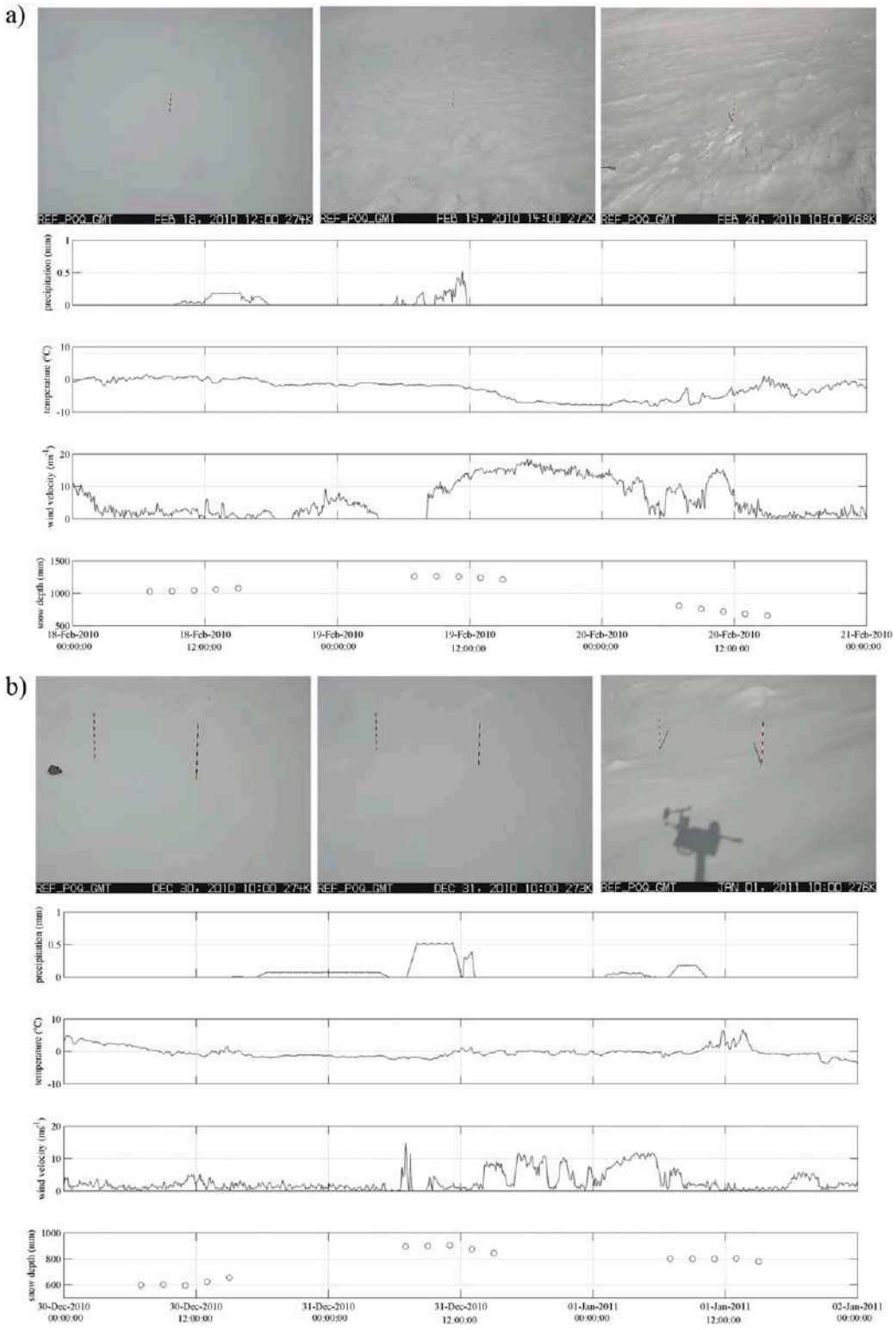

FIG. 8. Representation of TP images, weather data (5-min precipitation, temperature, and wind velocity), and measured snow depth during two periods where the assimilation results overpass the initial overestimation of the simulated snow depth: (a) from 18 to 21 Feb 2010 and (b) from 30 Dec 2010 to 2 Jan 2011.

assimilation techniques of snow maps for the simulation of their distribution at higher spatial scales than that of this work. On both these work lines, TP constitutes an economical and efficient complementary source of data to be combined with remote sensing sources for distributed snow modeling and provides the required resolution to provide information on the significant processes at the subgrid scale. The cost efficiency of TP makes this technique a feasible and convenient one to be included in conventional weather monitoring stations in mountainous areas in semiarid environments.

Acknowledgments. This work has been funded by the Spanish Ministry of Science and Innovation (Research Project CGL2011-25632, ''Snow dynamics in Mediterranean regions and its modeling at different scale. Implication for water resource management'').

REFERENCES

Anderson, E. A., 1976: A point energy and mass balance model of snow cover. NOAA Tech. Rep. NWS 19, 150 pp. [Available online at http://amazon.nws.noaa.gov/articles/HRL_Pubs_PDF_May12_2009/HRL_PUBS_51-100/81_A_POINT_ENERGY_AND_MASS.pdf.]

Anderson, R. S., G. Jiménez-Moreno, J. S. Carrión, and C. Pérez-Martínez, 2011: Postglacial history of alpine vegetation, fire and climate from Laguna de Río Seco, Sierra Nevada, southern Spain. *Quat. Sci. Rev.,* **30,** 1615–1629, doi:10.1016/j.quascirev.2011.03.005.

Bishop, C. H., B. Etherton, and S. J. Majumdar, 2001: Adaptive sampling with ensemble transform Kalman filer. Part I: Theoretical aspects. *Mon. Wea. Rev.,* **129,** 420–436, doi:10.1175/1520-0493(2001)129<0420:ASWTET>2.0.CO;2.

Blöschl, G., 1999: Scaling issues in snow hydrology. *Hydrol. Processes,* **13,** 2149–2175, doi:10.1002/(SICI)1099-1085(199910)13:14/15<2149::AID-HYP847>3.0.CO;2-8.

Buttle, J. M., and J. J. McDonnell, 1987: Modeling the areal depletion of snowcover in a forested catchment. *J. Hydrol.,* **90,** 43–60, doi:10.1016/0022-1694(87)90172-7.

Cline, D. W., R. G. Bales, and J. Dozier, 1998: Estimating the spatial distribution of snow in mountain basins using remote sensing and energy balance modeling. *Water Resour. Res.,* **34,** 1275–1285, doi:10.1029/97WR03755.

Corripio, J. G., 2004: Snow surface albedo estimation using terrestrial photography. *Int. J. Remote Sens.,* **25,** 5705–5729, doi:10.1080/01431160410001709002.

Dingman, L., 2002: *Physical Hydrology.* Prentice Hall, 600 pp.

Diodato, N., and G. Bellocchi, 2007: Modeling solar radiation over complex terrain using monthly climatological data. *Agric. For. Meteor.,* **144,** 111–126, doi:10.1016/j.agrformet.2007.02.001.

Evensen, G., 1994: Sequential data assimilation with a nonlinear quasi-geostrophic model using Monte Carlo methods to forecast error statistics. *J. Geophys. Res.,* **99,** 10 143–10 162, doi:10.1029/94JC00572.

Ferguson, R. J., 1984: Magnitude and modeling of snowmelt runoff in the Cairngorm mountains, Scotland. *Hydrol. Sci. J.,* **29,** 49–62, doi:10.1080/02626668409490921.

Fiume, L., 1989: *The Mathematical Structure of Raster Graphics.* Academic Press, 221 pp.

Foley, J. D., A. van Dam, S. K. Feimer, and J. F. Hughes, 1990: *Computer Graphics, Principles and Practice.* Addison-Wesley, 1175 pp.

Herrero, J., and M. J. Polo, 2012: Parameterization of atmospheric longwave emissivity in a mountainous site for all sky conditions. *Hydrol. Earth Syst. Sci.,* **16,** 3139–3147, doi:10.5194/hess-16-3139-2012.

——, ——, A. Moñino, and M. A. Losada, 2009: An energy balance snowmelt model in a Mediterranean site. *J. Hydrol.,* **371,** 98–107, doi:10.1016/j.jhydrol.2009.03.021.

——, ——, and M. A. Losada, 2011: Snow evolution in Sierra Nevada (Spain) from an energy balance model validated with Landsat TM data. *Remote Sensing for Agriculture, Ecosystems, and Hydrology XIII,* C. M. U. Neale and A. Maltese, Eds., International Society for Optical Engineering (SPIE Proceedings, Vol. 8174), 817403, doi:10.1117/12.898270.

Jordan, R. E., 1991: A one-dimensional temperature model for a snow cover: Technical documentation for SNTERERM.89. Special Rep. 91-16, Cold Region Research and Engineers Laboratory, U.S. Army Corps of Engineers, Hanover, NH, 61 pp.

——, E. L Andreas, and A. P. Makshtas, 1999: Heat budget of snow-covered sea ice at North Pole 4. *J. Geophys. Res.,* **104,** 7785–7806, doi:10.1029/1999JC900011.

Kalman, R. E., 1960: A new approach to linear filtering and prediction problems. *J. Basic Eng.,* **82,** 35–45.

Kolberg, S. A., and L. Gottschalk, 2006: Updating of snow depletion curve with remote sensing data. *Hydrol. Processes,* **20,** 2363–2380, doi:10.1002/hyp.6060.

Kustas, W. P., A. Rango, and R. Uijlenhoet, 1994: A simple energy budget algorithm for the snowmelt runoff model. *Water Resour. Res.,* **30,** 1515–1527, doi:10.1029/94WR00152.

Kuusisto, E., 1986: The energy balance of a melting snow cover in different environments. *IAHS Publ.,* **155,** 37–45. [Available online at http://iahs.info/uploads/dms/iahs_155_0037.pdf.]

Liston, G. E., R. A. Pielke, and E. M. Greene, 1999: Improving first-order snow-related deficiencies in a regional climate model. *J. Geophys. Res.,* **104,** 19 559–19 567, doi:10.1029/1999JD900055.

Luce, C. H., and D. G. Tarboton, 2004: The application of depletion curves for parameterization of subgrid variability of snow. *Hydrol. Processes,* **18,** 1409–1422, doi:10.1002/hyp.1420.

——, ——, and K. R. Cooley, 1999: Sub-grid parameterization of snow distribution for an energy and mass balance snow cover model. *Hydrol. Processes,* **13,** 1921–1933, doi:10.1002/(SICI)1099-1085(199909)13:12/13<1921::AID-HYP867>3.0.CO;2-S.

MacQueen, J. B., 1967: Some methods for classification and analysis of multivariate observations. *Proc. Fifth Symp. on Math, Statistics, and Probability,* Berkeley, CA, University of California, Berkeley, 281–297.

Malik, M. J., R. van der Velde, Z. Vekerdy, and Z. Su, 2012: Assimilation of satellite-observed snow albedo in a land surface model. *J. Hydrometeor.,* **13,** 1119–1130, doi:10.1175/JHM-D-11-0125.1.

——, ——, ——, and ——, 2014: Improving modeled snow albedo estimates during the spring melting season. *J. Geophys. Res. Atmos.,* **119,** 7311–7331, doi:10.1002/2013JD021344.

Marks, D., and J. Dozier, 1992: Climate and energy exchange at the snow surface in the alpine region of Sierra Nevada: 2. Snow cover energy balance. *Water Resour. Res.,* **28,** 3043–3054, doi:10.1029/92WR01483.

——, and A. Winstral, 2001: Comparison of snow deposition, the snow cover energy balance, and snowmelt at two sites in a semiarid mountain basin. *J. Hydrometeor.,* **2,** 213–227, doi:10.1175/1525-7541(2001)002<0213:COSDTS>2.0.CO;2.

Ott, E., and Coauthors, 2004: A local ensemble Kalman filter for atmospheric data assimilation. *Tellus,* **56A,** 415–428, doi:10.1111/j.1600-0870.2004.00076.x.

Painter, T. H., K. Rittger, C. Mckenzie, P. Slaughter, R. E. Davis, and J. Dozier, 2009: Retrieval of subpixel snow covered area, grain size, and albedo from MODIS. *Remote Sens. Environ.,* **113,** 868–879, doi:10.1016/j.rse.2009.01.001.

Pham, D., 2001: Stochastic methods for sequential data assimilation in strongly nonlinear systems. *Mon. Wea. Rev.,* **129,** 1194–1207, doi:10.1175/1520-0493(2001)129<1194:SMFSDA>2.0.CO;2.

Pimentel, R., J. Herrero, and M. J. Polo, 2012: Terrestrial photography as an alternative to satellite images to study snow cover evolution at hillslope scale. *Remote Sensing for Agriculture, Ecosystems, and Hydrology XIV,* C. M. U. Neale and A. Maltese, Eds., International Society for Optical Engineering (SPIE Proceedings, Vol. 8531), 85310Y, doi:10.1117/12.974419.

Reichle, R. H., 2008: Data assimilation methods in the earth sciences. *Adv. Water Resour.,* **31,** 1411–1418, doi:10.1016/j.advwatres.2008.01.001.

Rivera, A., J. G. Corripio, B. Brock, J. Clavero, and J. Wendt, 2008: Monitoring ice capped active VolcánVillarrica in southern Chile by mean of terrestrial photography combined with automatic weather stations and GPS. *J. Glaciol.,* **54,** 920–930, doi:10.3189/002214308787780076.

Rosenthal, W., and J. Dozier, 1996: Automated mapping of montane snow cover at subpixel resolution from the Landsat Thematic Mapper. *Water Resour. Res.,* **32,** 115–130, doi:10.1029/95WR02718.

Sade, R., A. Rimmer, M. I. Litaor, E. Shamir, and A. Furman, 2014: Snow surface energy and mass balance in a warm temperate climate mountain. *J. Hydrol.,* **519,** 848–862, doi:10.1016/j.jhydrol.2014.07.048.

Sakov, P., and P. R. Oke, 2008: Implications of the form of the ensemble transformation in the ensemble square root filters. *Mon. Wea. Rev.,* **136,** 1042–1052, doi:10.1175/2007MWR2021.1.

——, G. Evensen, and L. Bertino, 2010: Asynchronous data assimilation with the EnKF. *Tellus,* **62A,** 24–29, doi:10.1111/j.1600-0870.2009.00417.x.

Schulz, O., and C. de Jong, 2004: Snowmelt and sublimation: Field experiments and modelling in the high Atlas Mountains of Morocco. *Hydrol. Earth Syst. Sci.,* **8,** 1076–1089, doi:10.5194/hess-8-1076-2004.

Tarboton, D. G., and C. H. Luce, 1996: Utah Energy Balance Snow Accumulation Melt Model (UEB). Computer model technical description and user's guide, Utah Water Research Laboratory and USDA Forest Service Intermountain Research Station, 64 pp.

Tippett, M. K., J. L. Anderson, C. H. Bishop, T. M. Hamill, and J. S. Whitaker, 2003: Ensemble square root filters. *Mon. Wea. Rev.,* **131,** 1485–1490, doi:10.1175/1520-0493(2003)131<1485:ESRF>2.0.CO;2.

Wang, Z., and Coauthors, 2014: Evaluation of MODIS albedo product (MCD43A) over grassland agriculture and forest surface types during dormant and snow-covered periods. *Remote Sens. Environ.,* **140,** 60–77, doi:10.1016/j.rse.2013.08.025.